Cellulose (2022) 29:9549–9568
https://doi.org/10.1007/s10570-022-04856-4

ORIGINAL RESEARCH

# Molecular and crystal structures of cellulose in severely deteriorated archaeological wood

**Juan Guo · Jiabao Chen · Qiulu Meng · Leon Ploszczanski · Jian'an Liu · Rupeng Luo · Tao Jin · Philipp Siedlaczek · Helga C. Lichtenegger · Yafang Yin · Harald Rennhofer**

Received: 25 September 2021 / Accepted: 15 September 2022 / Published online: 16 October 2022


**Abstract** Preservation and conservation of archaeological wooden artifacts is extremely challenging due to a lack of knowledge about the hierarchical structure of preserved cellulose. Herein we report on the comparative analysis of eight archaeological and four recent wood samples from three archaeological sites in China by a variety of methods, including micromorphology, Fourier Transform Infrared Spectrum, X-ray scattering, chromatographic analysis of wood sugars, and solid state $^{13}C$ CP/MAS NMR. Results show that deterioration on the microscale is clearly related to a fragmentation of both the cellulose crystallite structure and the cellulose microfibrils. Slightly deteriorated archaeological wood features cellulose crystallites and microfibrils, comparable to non-degraded recent wood, whereas severely deteriorated wood shows higher porosity of the wood cell wall, fragmented cellulose aggregates instead of fibrils and nearly no crystallinity. Alterations in molecular structures resulted in advanced degradation of both amorphous and crystalline cellulose domains. Only a small amount of cellulose was preserved. The data allows to assume highly fragmented but still partially crystalline cellulose lamellas.

**Supplementary Information** The online version contains supplementary material available at https://doi.org/10.1007/s10570-022-04856-4.

J. Guo · J. Chen · Q. Meng · Y. Yin (✉)
Research Institute of Wood Industry, Chinese Academy of Forestry, Beijing 100091, China

J. Guo · J. Chen · Q. Meng · Y. Yin
Wood Collection of Chinese Academy of Forestry, Beijing 100091, China

Q. Meng
School of Resources, Environment and Materials, Guangxi University, No. 100 Daxue East Road, Nanning 530004, China

L. Ploszczanski · P. Siedlaczek · H. C. Lichtenegger · H. Rennhofer (✉)
Institute of Physics and Materials Science, Department of Material Sciences and Process Engineering, University of Natural Resources and Life Sciences, Vienna, 1190 Vienna, Austria
e-mail: harald.rennhofer@boku.ac.at

J. Liu · R. Luo
Zhejiang Provincial Institute of Cultural Relics and Archaeology, Jiaogong road No.71, Hangzhou 310012, Zhejiang, China

T. Jin
Ningbo Municipal Institute of Cultural Heritage Management, Baoshan Road No. 180, Ningbo 315012, Zhejiang, China

## Graphical abstract

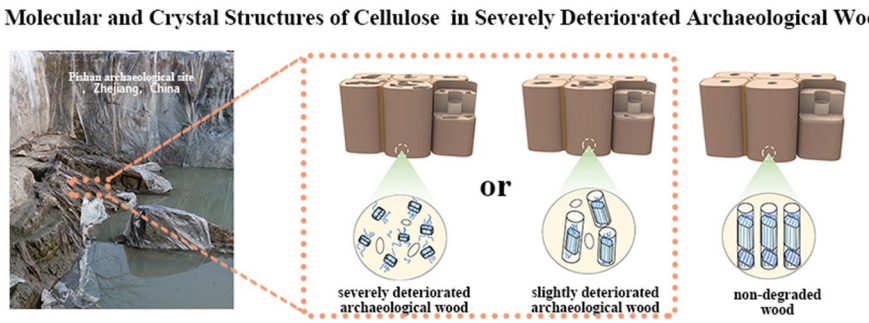


**Keywords** Archaeological wood · Cellulose · Molecular structure · Crystal structure · X-ray scattering

## Introduction

Archaeological wooden artifacts, running like a vein throughout human history (Glausiusz 2020), provide the sign of human-nature interactions (Liu et al. 2017), evidence the evolution of human technology (Conard et al. 2020) and reflect the humankind odyssey (Evershed et al. 1985). They could be retained in different preservation states, where the degradation of wood components is dependent on environments, burial periods, wood species and experienced processing treatments (Blanchette 2000; High and Penkman 2020). Moreover, the degradation process differs substantially with wood components hemicellulose, cellulose and lignin, despite similar buried environments (Pournou 2020). Therefore, analyzing molecular characteristics of archaeological wood is important in order to support archaeological practice and to contribute to the development of preventive conservation and remedial preservation of archaeological wooden artifacts (Nevin and Sawicki 2019).

Archaeological wood is characterized by the preferential loss of hemicellulose. Cellulose is not affected by degradation as strong as hemicellulose, due to the better stability of the cellulose crystallites. The relative amount of residual lignin is the highest, because lignin is resisting deterioration due to the unique phenolic, three-dimensional and cross-linked structure (Broda and Popescu 2019; Guo et al. 2019; Pedersen et al. 2021). Preservation of lignin in archaeological wood was studied extensively (Bardet et al. 2009; Colombini et al. 2009; Łucejko et al. 2012; Pizzo et al. 2015; Zoia et al. 2017; Guo et al. 2020; Han et al. 2020a; Lucejko et al. 2021; Pedersen et al. 2021). Lignin may experience a partial breakage of β-O-4 interlinks, demethylation of the methoxy group and oxidation, with the production of a higher concentration of free phenol groups, followed by the degradation of Lignin-Carbohydrate Complexes. However, the molecular and crystalline structure of cellulose in deteriorated wood was less studied although it is a key factor for determining the strength and dimensional stability of wooden artifacts (Bjurhager et al. 2012; Almkvist et al. 2016; Han et al. 2020a, b).

Cellulose, a linear macromolecular chain of 1,4-linked β-D-glucopyranose, self-assembles into long fibrils with nanosized diameters during the xylem cell differentiation (Terrett et al. 2019). Cellulose structural complexity becomes more comprehensive and profound in archaeological wood by abiotic and biotic mechanisms (Howell et al. 2007). The structural hierarchy of the wood cell wall changes with the preservation state of archaeological wood (Giachi et al. 2003; Li et al. 2014; Zhou et al. 2018; Broda and Popescu 2019; Han et al. 2020a). In slightly deteriorated archaeological wood, the degradation occurs predominantly to amorphous cellulose, only a slight change is detected in the crystal structure of cellulose (Sandak et al. 2010; Romagnoli et al. 2018; Han et al. 2020b). In severely deteriorated wood, cellulose in both amorphous and crystalline regions are reported to be degraded (Li et al. 2014; Broda and Popescu 2019; Guo et al. 2019; Ghavidel et al. 2020). This can be detected by e.g. much

broader and weaker crystalline diffraction bands, disoriented crystalline celluloses and the significant decrease in the crystallinity. In contrast with the typical X-ray pattern of cellulose $I_\beta$, measured also for slightly deteriorated archaeological wood, seriously cellulose degradation results in a changed scattering pattern. The characteristic diffraction peaks of cellulose $I_\beta$ corresponding to the (1–10) and (110) crystallographic planes and even (004) crystallographic planes are unrecognizable after degradation, the visible diffraction peak attributed to (200) planes becomes wider and weaker (Broda and Popescu 2019; Ghavidel et al. 2020). To the knowledge of the authors there is no dedicated study addressing the changes of hierarchical structure of cellulose in severely deteriorated archaeological wood, including crystal structure, chemical and morphological information.

The aim of this research was to link information on the molecular and crystal structures of cellulose in severely deteriorated archaeological wood. Therefore, six samples of severely deteriorated archaeological wood, two samples of slightly deteriorated archaeological wood and four non-degraded wood samples of relevant species were selected for a comparative analysis. The preservation state of the samples was investigated by several complementary methods: physical indexes, micromorphology and chemometrics were performed. Chromatographic analysis of wood sugars was conducted to quantify and identify the change of cellulose and hemicellulose in archaeological wood. The use of solid state $^{13}C$ CP/MAS nuclear magnetic resonance (NMR), Fourier Transform Infrared Spectrum (FTIR) and the small-angle and wide-angle X-ray diffraction (SAXS/WAXD) provides access to cellulosic molecular and crystal structure traits, including molecular structure of cellulose, lattice and dimension of cellulose crystallites, arrangement and size of fibrils, as well as pores between fibrils.

## Materials and methods

### Materials

Eight waterlogged archaeological wood samples from three excavation sites were collected. Wood identification was carried out by a light microscope (Olympus BX51, Japan) on polyethyl glycol 2000 embedded wood sections with a thickness of 15 µm. Anatomical descriptions were based on the terminology proposed by the International Association of Wood Anatomists Committee (IAWA committee 1989; IAWA committee 2004). Four non-degraded recent wood samples of

**Table 1** The list of the examined wood samples

| Sample name | Species | Source | Age (approx.) | Maximum water content, MWC (%)[a] | Basic density, BD ($g \times cm^{-3}$)[b] |
|---|---|---|---|---|---|
| *C1* | *Quercus* sp. | Wooden dam in the Pishan archaeological site, Zhejiang, China | 2900–2500 BC | 152 ± 16 | 0.492 |
| *C2* | *Quercus* sp. | | 2900–2500 BC | 346 ± 18 | 0.239 |
| *C3* | *Quercus* sp. | | 2900–2500 BC | 247 ± 13 | 0.313 |
| *C4* | *Ulmus* sp. | | 2900–2500 BC | 407 ± 30 | 0.225 |
| *C5* | *Populus* sp. | | 2900–2500 BC | 120 ± 24 | 0.569 |
| *C6* | *Cunninghamia* sp. | Pishan archaeological site, Zhejiang, China | 960–1279 AD | 127 ± 13 | 0.522 |
| *C7* | *Cunninghamia* sp. | Shipwreck in the Wanjiao No.1, Fujian, China | 1680–1700 AD | 523 ± 42 | 0.252 |
| *C8* | *Cunninghamia* sp. | | 1680–1700 AD | 487 ± 40 | 0.217 |
| *C9* | *Quercus* sp. | Chosen from Wood Collection, Chinese Academy of Forestry | Recent | | |
| *C10* | *Ulmus* sp. | | | | |
| *C11* | *Populus* sp. | | | | |
| *C12* | *Cunninghamia* sp. | | | | |

[a]Maximum Water Content, MWC (%): percentage ratio of the difference between masses of water-saturated wood (M) and freeze-dried wood ($M_0$), three duplications were used, $MWC = (M\text{-}M_0)/M_0 \times 100$;

[b]Basic Density, BD ($g \times cm^{-3}$): ratio between freeze-dried wood mass ($M_0$) and volume of water-saturated wood (V)

relevant species were additionally studied as a reference. Details on wood species, archaeological contexts and the physical analyses are given in Table 1.

Scanning electron microscopy (SEM)

Thin sections of waterlogged archaeological wood were obtained with a cryostat (CM3050S, Leica, Germany). They were dehydrated with a series of ascending ethanol concentrations and supercritical $CO_2$ dried by a critical point drier (EM CPD300, Leica, Germany) to avoid shrinkage due to capillary pressure. The supercritical $CO_2$ drying was performed with a pressure of 9.5 MPa, a temperature of 40 °C, a flow rate of 40 g $min^{-1}$ for 3–4 h. The dried samples were mounted with high purity conductive double sided adhesive carbon tabs on aluminum stubs, sputter-coated with 10 nm gold (Scancoat Six; Edwards, UK) and observed using a FEI Quanta 250 FEG ESEM (Thermo Fisher Scientific, USA) at an accelerating voltage of 20 kV in high vacuum condition, with a spot size of 3.0 and using the SE ETD detector.

*Fourier transform infrared spectrometer (FTIR) coupled with chemometrics*

The KBr pellet technique was applied: waterlogged archaeological wood was freeze-dried using a vacuum freeze-drying equipment (FD-1A-50, Boyikang Company, China). FTIR spectra of dried wood samples pelletized with KBr powder were recorded with a FTIR spectrometer Frontier (PerkinElmer, UK). 64 scans were carried out with a 4 $cm^{-1}$ spectral resolution in the range 4000–400 $cm^{-1}$. The samples were analyzed in triplicate. Spectra were normalized before further evaluation in the range 1850–400 $cm^{-1}$, by means of the minimum–maximum normalization.

Principal component analysis (PCA) was used on the fingerprint region in the 1850–830 $cm^{-1}$ for distinguishing the similarities and dissimilarities among FTIR spectra of different wood samples by SIMCA software (Umetrics, Sweden). Moreover, the loading plot allows for identifying important spectral bands that account for the most significant differences.

FTIR indexes were calculated according to previous studies for quantitative analysis (Faix 1991; Pandey and Pitman 2003; Darwish et al. 2013; Cavallaro et al. 2019; Guo et al. 2019; Pozhidaev et al. 2019; Lucejko et al. 2020). The lignin index was estimated by the ratio between the absorption intensities at 1592 $cm^{-1}$ and 1505 $cm^{-1}$. The carbohydrates/lignin index was estimated by the ratio between the absorption intensities at 1374 $cm^{-1}$ and 1505 $cm^{-1}$.

Sugar composition analysis

Wood samples were freeze-dried followed by a freeze-grinding treatment using an EFM Freezer Mill 6770 (SPEX SamplePrep, Metuchen, USA). The dry mass of archaeological wood *C5, C7* and *C11* was not sufficient, thus *C5*, *C7* and *C11* were not used for sugar composition analysis. Samples were extracted with 2:1 benzene ethanol in a Soxhlet apparatus for 8 h and then kept at room temperature to dry. Subsequently, from the resulting dry mass of about 300 mg, sugar solutions were prepared following a NREL method (Sluiter et al. 2012). In short, the samples were hydrolyzed for 1 h at 30 °C in 72% $H_2SO_4$, then diluted to 3% $H_2SO_4$ and hydrolyzed for 1 h at 120 °C in the autoclave. The samples were filtered through a 0.22-µm membrane and diluted for the analysis by high-performance liquid chromatography (HPLC) (ICS5000, Thermo Fisher Scientific, USA) on a CarboPac PA-20 anion-exchange column (150×3.0 mm, 10 µm, Dionex) using a pulsed amperometric detector (PAD, Dionex ICS 5000 system). The experimental condition was set at a flow rate of 0.5 mL/min, an injection volume of 5 µL, a solvent system of 0.1 M NaOH (flow phase A) and 0.1 M NaOH and 0.2 M NaAc (flow phase B), and a gradient program of 95:5 $V_A/V_B$ at 0 min, 80:20 $V_A/V_B$ at 30 min, 60:40 $V_A/V_B$ at 30.1 min, 60:40 $V_A/V_B$ at 45 min, 95:5 $V_A/V_B$ at 45.1 min, 95:5 $V_A/V_B$ at 60 min. A series of calibration standards were prepared, containing the compounds to be quantified, including fucose, rhamnose, arabinose, galactose, glucose, xylose, mannose, fructose, ribose, galacturonic acid, glucuronic acid, mannuronic acid and guluronic acid, which were purchased from the Sigma Company (USA). Data was processed using chromeleon 7.2 CDS (Thermo Scientific, USA).

Solid state ***$^{13}$C cross-polarization (CP)/magic angle spinning (MAS) NMR spectra***

Freeze-grinded wood powder of *C1–C3*, *C6*, *C8–C11* was used to acquire solid state $^{13}$C CP/MAS NMR spectra by an Avance III 400 WB NMR spectrometer

(Bruker, Billerica, USA) operating at 100.62 MHz. A sample spinning speed of 7 kHz was used. $^{13}$C NMR experiments were performed with a 2 ms contact time, a 33 ms acquisition time and a 5 s relaxation delay. Freeze-grinded wood powder of *C4* was measured by an Avance III 400 HD NMR spectrometer (Bruker, Billerica, USA) operating at 100.625 MHz. A sample spinning speed of 10 kHz was used. $^{13}$C NMR experiments were performed with a spectral width of 30 kHz and 15 µs between repeats. 1024 data complex points were acquired in 1 h. Chemical shift values were measured with respect to glycine as a reference with the carbonyl signal set at 38.5 ppm.

### Small-angle X-ray scattering (SAXS) and wide-angle X-ray diffraction (WAXD)

Tangential wood slices with the thickness of 0.8 mm were cut directly by hand from each wood sample. They were dried at 37 RH%, 21 °C in a closed humidity chamber. Small-angle X-ray scattering (SAXS) and wide-angle X-ray diffraction (WAXD) experiments were performed on a RIGAKU S-Max3000 machine with MM002 + Cu-$K_\alpha$ source (wavelength $\lambda = 0.154$ nm). Scattered intensity was detected on a Triton200 multi wire detector (SAXS) at about 500 mm distance from the sample and a Fuji Image Plate system (WAXD) at about 25 mm from the sample. Measurement times were 1200–3600 s for one SAXS image and 1800s for one WAXD image. The measurement time for one SAXS image was dependent upon the scattering intensity of each wood specimen. The X-ray beam size was determined by a three-pinhole system after the X-ray optics and the beam diameter was about 400 µm (circular) on the sample. The X-ray beam was oriented perpendicular to the fiber axis of the samples, i.e. hitting the wood samples in radial direction. For better statistics two different positions in each wood specimen were chosen, measured and evaluated. The final results were averaged, thus values displayed in the diagrams are mean values of two individual measurements. Individual errors resulted from the fit, errors displayed are the error of the averaged value taking these into account.

The scattering images were integrated and background corrected by subtraction of the signal of the empty sample holder before further data evaluation. Azimuthal integration was applied to obtain scattered intensity I(q) as a function of the length of the scattering vector q. For convenience the SAXS curves were depicted in I(q), while the WAXD curves were showing I(2θ). The q range in SAXS was 0.3–8 $nm^{-1}$ and the 2θ-range in WAXD was 10–40° 2θ (for Cu-$K_\alpha$). The following equation related wavelength λ of the X-rays, the scattering vector q and the scattering angle 2θ:

$$q = \frac{4\pi}{\lambda} \cdot \sin\theta \tag{1}$$

Dimensions of cellulose crystallites were analyzed from the width of the diffraction peaks in WAXD using Origin (OriginLab Corportion, UK), assuming Gaussian functions for all peaks. The average dimension ($L_{hkl}$) of cellulose crystallites was calculated from the full width at half maximum (FWHM) of the Bragg peaks using the Scherrer formula (Eq. 2), with

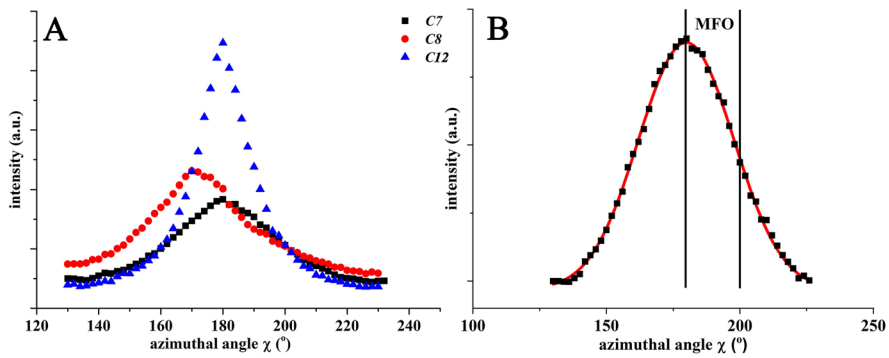


**Fig. 1** **A** Scattering curves I(χ) of archaeological *Cunninghamia* wood *C7* (black squares) *and C8* (red circles) and non-degraded recent *Cunninghamia* wood *C12 (blue triangles).* **B** The scattering curve of *C7* (black squares), single Gaussian shaped curve used for the fit (red line) and microfibril orientation distribution (MFO) indicated by solid black lines

λ the wavelength of the X-rays (0.154 nm) and 2θ the angle where the diffraction peak occurred.

$$L_{hkl} = \frac{0.89 \times \lambda}{\cos\theta \times FWHM} \quad (2)$$

The SAXS images were also integrated radially and plotted as function of the azimuthal spread I(χ), allowing to access the angular distribution of microfibrils of cellulose fibrils in wood cell walls (Lichtenegger et al. 1999). The peak can be fitted by one single Gaussian function, in which case only microfibrils orientation (MFO) can be obtained, defined by the half width at half maximum of this Gaussian distribution. Figure 1A displays I(χ) for three different samples, the definition of the angular distribution is indicated in Fig. 1B. Scattering curves I(χ) of wood samples *C7–C12* were present in supporting information (Fig. S1).

The diameter and diameter distribution of the fibrillar structure of wood samples were evaluated from the minimum in the SAXS scattering curve at about 3 $nm^{-1}$, following the published literature (Jakob et al. 1995). A fit was applied to the scattering curve assuming cylindrically shaped cellulose fibrils with a Gaussian size distribution and a hard sphere structure factor, taking an additional $q^{-4}$ contribution into account. The fitting process was carried out using the software SASfit (Breβler et al. 2015) to obtain values of mean fibril diameter ($D_0$), the diameter distribution (σ) and the average fibril distance ($D_f$) from the hard sphere radius. The fit was applied to data of *C7–C12* in the range of about q = 0.7–5 $nm^{-1}$.

The correlation length ($l_{CH}^*$) parameter qualitatively describes structural changes as an estimate of the intensity-averaged electron density fluctuations (Glatter and Kratky 1982; Ehmann et al. 2015). It is calculated based on the integral of the scattering profile, hence is less prone to noisy data.

$$l_{CH}* = \frac{\pi}{Q} \cdot \int_{q_{min}}^{q_{max}} I(q) \cdot q \, dq \quad where \quad Q = \int_{q_{min}}^{q_{max}} I(q) \cdot q^2 \, dq \quad (3)$$

where $l_{CH}^*$ is the mean correlation length estimate, Q is the invariant. Unit of $l_{CH}^*$ is nanometer (nm).

Pore structure was analyzed using the SAXS scattering curve. The radius of gyration ($R_g$) of pores and the fractal dimension (n) of these pores, were chosen

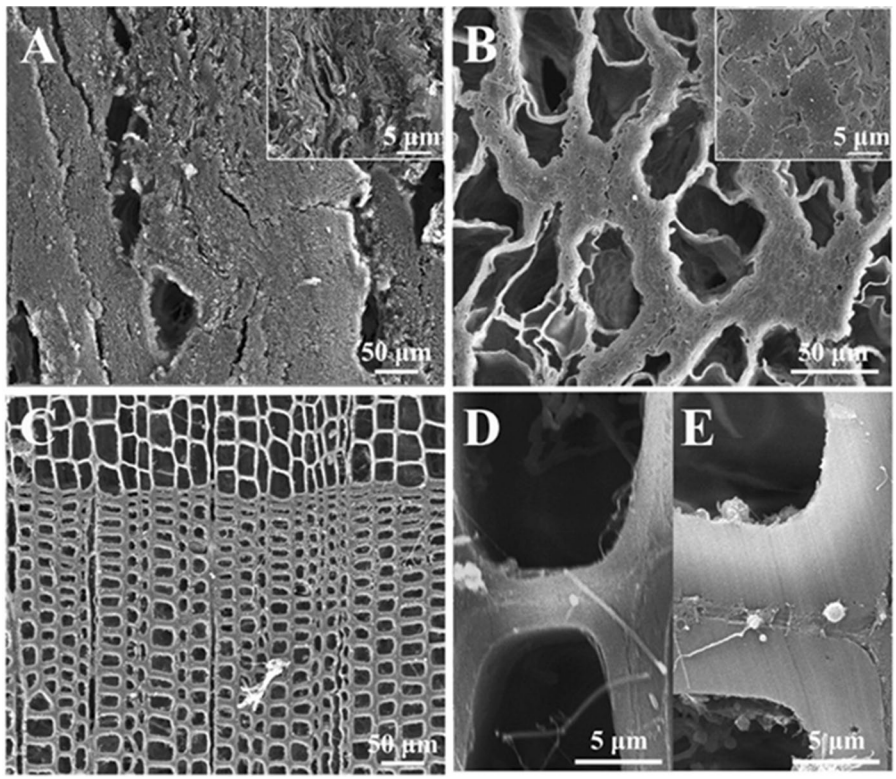


**Fig. 2** ESEM micrographs of cross sections of archaeological wood **A** *Quercus* (*C1*), **B** *Populus* (*C5*) and **C** *Cunninghamia* (*C7*). Magnifications of cell walls are inserted in the right top corners of **A, B**. Cell walls of early- and latewood of *C7* are shown in D and E

as parameters reflecting the change in the scattering curves in the low-q regime. The curvature in the low-q region of 0.38–0.55 $nm^{-1}$ was evaluated by the Guinier approximation (Guinier and Fournet 1955), providing the information of $R_g$. This curvature is followed at higher q values by a power law, i.e. $I(q) \sim q^{-n}$, where the exponent *n* can be attributed to the fractal dimension of the system, related to surface characteristics of these nano-pores (Teixeira 1988). The exponent *n* would be between 3 and 4 for surface fractals and between 1 and 3 for volume fractals. Here *n* was evaluated in the range from $q = 0.45–0.65\ nm^{-1}$.

## Results and discussion

### Preservation state of studied archaeological wood

The preservation state of the cellulose structures in archaeological wood is fundamental. To assess the state, multidisciplinary methods including the MWC and BD criteria, micromorphology and Fourier Transform Infrared Spectrum (FTIR) coupled with chemometrics were used to evaluate the preservation state. The average MWC and BD values of waterlogged archaeological wood *C1–C6* ranges from 120 to 407%, and from 0.225 to 0.569 $g \times cm^{-3}$ (Table 1). *C7* and *C8*, whose burial periods were much shorter than *C1–C6*, have higher MWC values of 523% and 487%, and lower BD values of 0.217 and 0.252 $g \times cm^{-3}$, respectively. By comparing their MWC and BD values, *C7* and *C8* would be in a worse preservation state than *C1–C6*. Micromorphological features were also used to evaluate the preservation state. Representative SEM micrographs of *C1*, *C5* and *C7* are shown in Fig. 2. Structure collapses are obvious in *C1* and *C5*. Cells have lost their original shapes and display are distorted. *C7* shows little evidence of decay, despite fungal colonization of the cell walls (Fig. 2C). The majority of early- and latewood tracheids remains

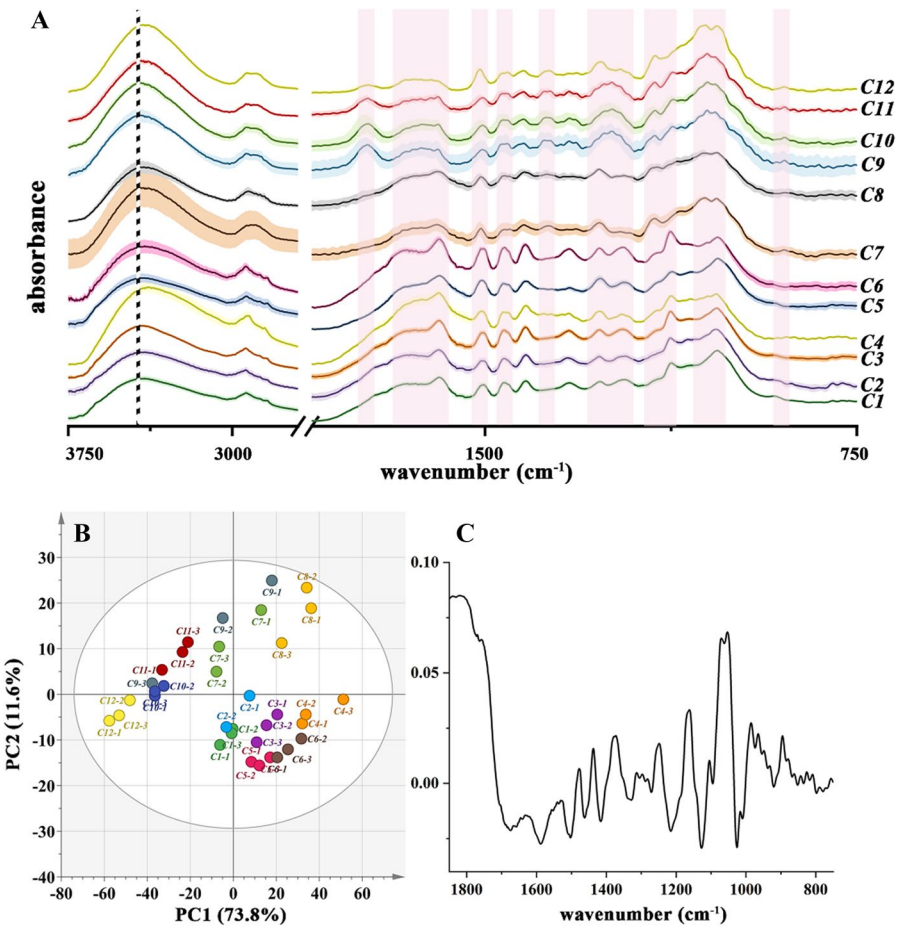


**Fig. 3** **A** Normalized average FTIR spectra of dried archaeological wood (*C1–C8*) and non-degraded recent wood (*C9–C12*), PCA scores **B** and the loading plot **C** of PC2 of samples *C1–C12*. Peak assignments for FTIR spectra are listed in Table S1

intact (Fig. 2D). Thus, from microscopy, *C7* and *C8* seem to be in a better preservation state than *C1–C6*, which is contradictory to the evaluation results by the MWC and BD.

FITR analysis

Hence, FTIR spectra assisted with chemometrics were further used to analyze the preservation state (Macchioni et al. 2012; Pizzo et al. 2015; Traoré et al. 2016). The normalized average FTIR spectra are shown in the Fig. 3A. Distinct spectral differences can be seen between archaeological and non-degraded wood samples. The absence of the band at 1740 $cm^{-1}$ mainly ascribed to C=O stretching of acetyl and carbonyl groups in hemicellulose (Table S1, in the supporting information), was found in all spectra of archaeological wood. It revealed that the acetyl side chains of hemicellulose were preferentially degraded. There are spectral differences between *C1–C6* and *C7*, *C8*, namely in the band assigned to lignin (1665, 1592, 1505, 1462, 1420, 1330, 1270, 1214, 1126 and 1030 $cm^{-1}$) and the bands assigned to carbohydrates (1374, 1158, 1052 and 896 $cm^{-1}$). *C1–C6* feature higher relative intensities of the lignin bands and lower relative intensities in the carbohydrate bands, compared to samples *C7* and *C8* (Table S1). This indicates deterioration of carbohydrates with respect to lignin is more intense in *C1 – C6* than in *C7*, *C8*. Several other features indicate decomposition of carbohydrates as well: the characteristic C–O stretching and C–O–C stretching bands at 1052 and 1158 $cm^{-1}$ show a strong decrease of intensities for *C1–C6* (Fig. 3A). The spectral intensity ratios $I_{1374}/I_{1505}$ of the carbohydrate band at 1374 $cm^{-1}$ and the lignin band at 1505 $cm^{-1}$ show identical values for recent wood samples and *C7* and *C8*, whereas *C1–C6* feature lower values. This indicates only slight degradation of carbohydrates in *C7* and *C8* and severe degradation in *C1–C6*.

**Table 2** Cellulosic molecular and crystal structure traits analyzed by FTIR absorption bands and solid state $^{13}C$ CP/MAS NMR

| | FTIR | | Solid state $^{13}C$ CP/MAS NMR | | |
|---|---|---|---|---|---|
| | $I_{1592}/I_{1505}$ [a] | $I_{1374}/I_{1505}$ | $A_{154}/A_{148}$ [b] | $A_{105}/A_{56}$ | $A_{88.7}/A_{83.8}$ |
| *C1* | 1.2 ± 0.02 | 0.9 ± 0.01 | 17.9 | 0.3 | 0.02 |
| *C2* | 1.3 ± 0.03 | 0.9 ± 0.02 | 4.5 | 0.1 | 0.02 |
| *C3* | 1.3 ± 0.02 | 0.9 ± 0.01 | 9.3 | 0.3 | 0.1 |
| *C4* | 1.3 ± 0.04 | 0.9 ± 0.01 | 1.1 | 0.4 | 0.4 |
| *C5* | 1.1 ± 0.01 | 0.8 ± 0.01 | nd[c] | nd | nd |
| *C6* | 1.2 ± 0.02 | 0.8 ± 0.01 | 7.1 | 0.3 | 0.1 |
| *C7* | 1.1 ± 0.04 | 1.1 ± 0.1 | nd | nd | nd |
| *C8* | 1.1 ± 0.04 | 1.1 ± 0.03 | 1 | 4.7 | 0.2 |
| *C9* | 1.0 ± 0.01 | 1.3 ± 0.1 | 3.2 | 1.5 | 0.3 |
| *C10* | 1.0 ± 0.01 | 1.1 ± 0.01 | 3.4 | 1.5 | 0.2 |
| *C11* | 1.0 ± 0.03 | 1.2 ± 0.02 | nd | nd | nd |
| *C12* | 0.6 ± 0.03 | 1.1 ± 0.02 | 0.9 | 1 | 0.2 |

[a]The spectral intensity ratio of bands;

[b]The integral area ratio of resonances;

[c]nd: not measured, because the dry mass of archaeological wood *C5* and *C7* was not sufficient for solid state $^{13}C$ CP/MAS NMR measurements;

The spectral intensity ratio between the bands at 1592 and 1505 $cm^{-1}$ $I_{1592}/I_{1505}$ gives information on the molecular structure of aromatic lignin. In the spectrum of non-degraded recent *Cunninghamia* softwood *C12*, the $I_{1595}/I_{1505}$ ratio is 0.6, while hardwoods feature a ratio of 1.0. This is attributed to species variations in lignin, in specific to a higher content of guaiacyl units in softwoods (Sarkanen et al. 1967). $I_{1592}/I_{1505}$ in general is increasing for archaeological wood (Table 2), indicating the oxidation of aromatic lignins, the loss of guaiacyl units, or most likely the demethoxylation of guaiacyl units. Oxidation of glucopyranose rings and the oxidation of phenolic compounds in lignin is also indicated by the broadening of the carbonyl band at 1660 $cm^{-1}$ (Darwish et al 2013).

To support this result a separate principal component analysis (PCA) based on the 1850–750 $cm^{-1}$ spectral range was obtained (Fig. 3B). It is shown in the scores plot of PC1 and PC2, which account for 85.4% of data variability. Along the PC2 axis, the upper side of plot shows the cluster of archeological wood *C7*, *C8* and recent wood *C9–C12*, and the downside depicts archaeological wood *C1–C6*. *C7* and *C8* are further separated from *C9–C12* in the score plot of PC1. Important FTIR spectral bands relating to the wood deterioration can be classified in the loading plot of PC2 (Fig. 3C). The PC2 loading shows the positive absorbance mainly from carbohydrates bands peaked at 1750, 1374, 1162, 1058 and 896 $cm^{-1}$, as well as the negative absorbance from

**Table 3** Sugar composition (%)[a] of benzene ethanol extracted archaeological and non-degraded wood samples as determined by HPLC[b, c]

| | Total sugar | Glc[d] | Ara | Gal | Xyl | Man |
|---|---|---|---|---|---|---|
| *C1* | 5.8 ± 0.2 | 2.3 ± 0.04 | 0.6 ± 0.02 | 1.3 ± 0.1 | 0.5 ± 0.02 | 0.1 ± 0.01 |
| *C2* | 17.3 ± 0.4 | 10.8 ± 0.2 | 0.6 ± 0.02 | 1.4 ± 0.04 | 1.9 ± 0.1 | 1.5 ± 0.1 |
| *C3* | 4.8 ± 0.02 | 1.9 ± 0.02 | 0.5 ± 0.004 | 1.2 ± 0.004 | 0.3 ± 0.003 | 0.09 ± 0.001 |
| *C4* | 20.4 ± 1.8 | 12.8 ± 1.1 | 0.3 ± 0.02 | 1.1 ± 0.06 | 4.5 ± 0.5 | 0.3 ± 0.02 |
| *C6* | 8.2 ± 0.2 | 4.5 ± 0.1 | 0.4 ± 0.02 | 1.0 ± 0.02 | 0.9 ± 0.03 | 0.2 ± 0.01 |
| *C8* | 49.6 ± 1.2 | 36.7 ± 0.9 | 0.1 ± 0.01 | 1.2 ± 0.04 | 2.7 ± 0.1 | 8.0 ± 0.2 |
| *C9* | 42.5 ± 0.5 | 24.0 ± 0.2 | 0.6 ± 0.03 | 0.8 ± 0.02 | 14.2 ± 0.2 | 1.5 ± 0.05 |
| *C10* | 52.6 ± 1.3 | 34.5 ± 0.8 | 1.1 ± 0.04 | 1.4 ± 0.07 | 12.7 ± 0.3 | 0.8 ± 0.03 |
| *C12* | 25.1 ± 0.4 | 17.9 ± 0.1 | 0.3 ± 0.03 | 0.7 ± 0.1 | 2.0 ± 0.04 | 3.9 ± 0.08 |

[a]Data are expressed as a percentage based on dry weight of benzene ethanol extracted wood samples;

[b]Data are mean values of duplicate analysis ± standard deviation;

[c]Percentages of fucose, rhamnose, galacturonic acid, guluronic acid and glucuronic acid were present in supporting information (Fig. S2);

[d]Glc: glucose; Ara: arabinose; Gal: galactose; Xyl: xylose; Man: mannose

lignin bands peaked at 1673, 1592, 1505, 1462, 1420, 1330, 1270, 1214, 1126 and 1025 $cm^{-1}$ (Fig. 3C).

On the basis of MWC and BD values, micromorphological features, FTIR spectra and related PCA analysis of FTIR spectra, *C1–C6* were considered to be the severely deteriorated archaeological wood, and *C7*, *C8* were evaluated to be slightly deteriorated archaeological wood.

## Sugar composition analysis

The sugar compositions of archaeological wood and non-degraded wood were analyzed (Table 3). The total hydrolysis of recent wood yields, dependent on the species, about 25–53% sugar, deteriorated archaeological wood samples yield less, *C8* about 50% and *C1–C6* about 5–20% sugar. It indicates, that the sugars of severely deteriorated archaeological wood were degraded more extensively than those of slightly deteriorated archaeological wood.

Glucose can be found in cellulose and hemicellulose. We are analytically unable to distinguish cellulosic and hemicellulosic glycans (Geng et al. 2019), thus, the glucose content presented here is the upper bound of the cellulose content. The predominant hemicellulose type in hardwoods and softwoods is glucuronoxylan and galactoglucomannan, respectively. Thus, comparing the relative amounts significant differences in NMR spectra of glucose, xylose and mannose with respect to total amount of sugars in each sample (set to 100/100 parts), can give more detailed information on the decay. The glucose, xylose and mannose accounted e.g. for about 72/100, 8/100 and 16/100 of the total sugars in *C12*, also 74/100, 6/100 and 16/100 in *C8* but only 33/100, 8/100 and 2/100 in *C1*, respectively. We find, that slightly deteriorated archaeological wood has similar cellulose and hemicellulose content compared to non-degraded wood of the same species. However, severely deteriorated archaeological wood shows not only less sugar, but a more complex final sugar composition. *C2* features, compared to samples *C1* and *C3* of the same species, a higher glucose content (65/100), comparable xylose content (12/100) and higher mannose content (8/100) of total sugars. *C4,* excavated from the same archaeological site as *C1–C3* had with 63/100, 22/100 and 5/100 a comparable glucose, xylose and mannose proportion as the non-degraded reference wood *C10* (66/100, 25/100 and 3/100). It is known, that degradation depends a lot on the condition and species (Lucejko et al. 2020; Pournou 2020; Zhou et al. 2018). The results suggest, that different decay mechanisms might be operating. Archaeological wood *C1–C6* all show a relative increase in galactose content (5/100–25/100), in comparison with non-degraded woods (about 3/100), see

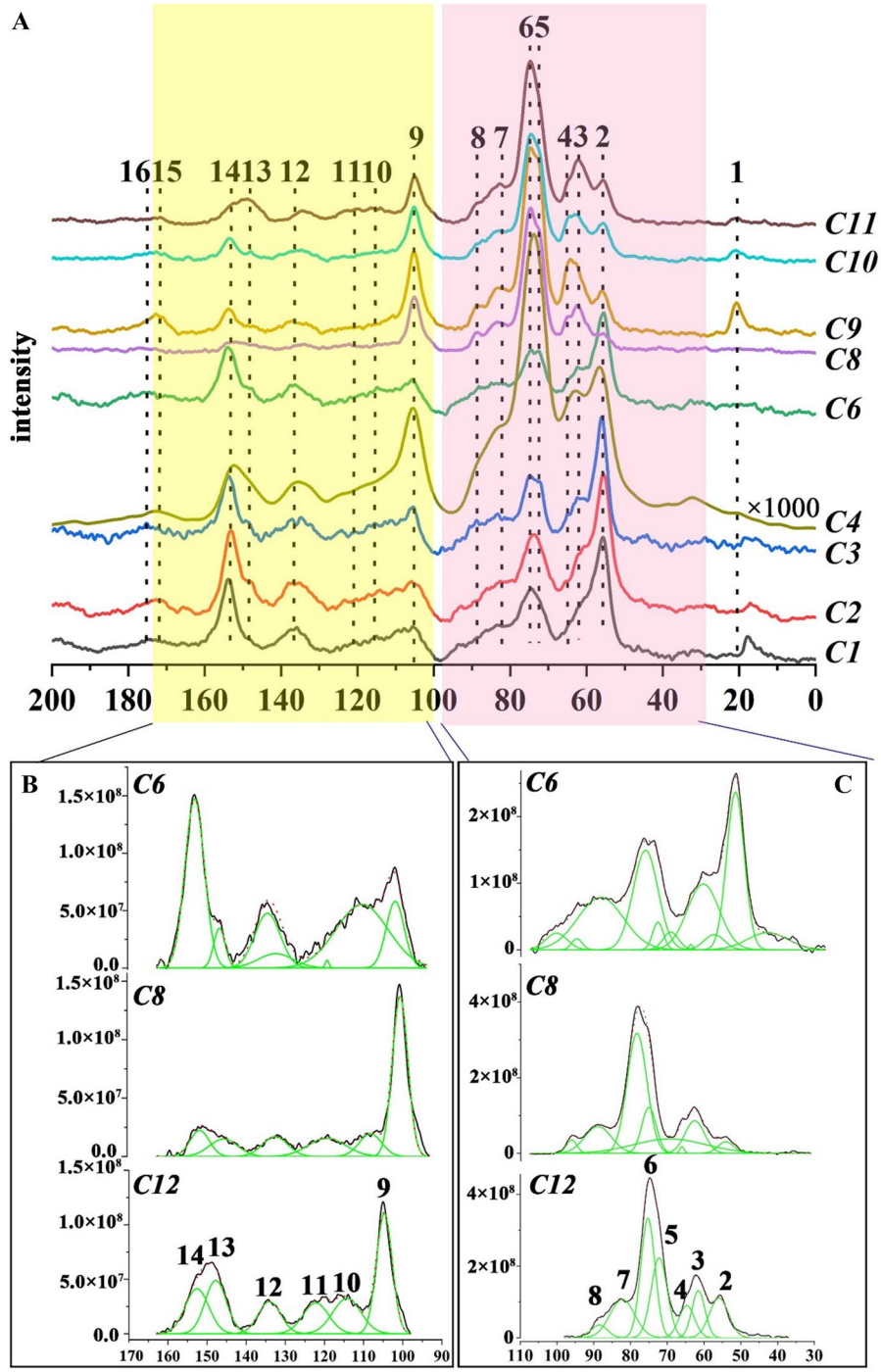


**Fig. 4** The solid state $^{13}C$ CP/MAS NMR spectra of wood samples. **A** Full spectra of *C1–C4*, *C6*, *C8–C10* and *C12*, **B, C** magnification of the two regions of the NMR spectra. For clarity, the deconvoluted spectra colored with the green overlapped with the experimental ones, the black lines, and the cumulative fitting lines are red dotted lines

Table 3, which could hint towards fungal influence during decay, since galactose is also a fungal cell wall component (Anagost et al. 1994).

The sum of xylose, galactose, arabinose and mannose contents can be considered to represent the hemicellulose content (Geng et al. 2019). The overall content was reduced from about 8–17% in recent wood to only 2–6% for severely degraded wood. The relative amount of hemicellulose with respect to total amount of sugars was comparable between the

reference samples of each species (28/100–40/100) and the according degraded wood (30/100–45/100). This shows extensive degradation of glucose and hemicelluloses in severely deteriorated archaeological. Nevertheless, the relative loss of hemicellulose with respect to the total sugar amount is comparable to the glucose loss, indicating degradation of cellulose (glucose) and hemicellulose to the same extent. Hemicellulose plays an important role in the cell wall matrix, in binding to amorphous cellulose and to the surface of cellulose microfibrils in a semi-crystalline domain (Terrett et al. 2019). The reduced hemicellulose content inevitably promoted a change in cellulose aggregates, including their molecular arrangement, orientation, distance and interfacial structure. The actual molecular structure of cellulose in archaeological wood is investigated by FTIR (see above) and solid state $^{13}$C CP/MAS NMR (below).

### $^{13}$C CP/MAS NMR

$^{13}$C CP/MAS NMR spectra of archaeological wood show several differences with respect to recent wood: significant gain of intensities in the lignin aromatic region (160–106 ppm), a gain in the resonance 56 ppm arising from methoxyl substituents in lignin, a significant decrease and alterations in the carbohydrate region (105–65 ppm), absences of the resonances at 21 ppm and 172 ppm, ascribed to the $CH_3$ and the carbonyls of acetyl groups in hemicellulose, respectively (Fig. 4A). The assignments of the $^{13}$C CP/MAS spectrum are listed in Table S3. This confirms the loss of hemicellulose and a higher relative amount of residual lignin in archaeological wood, which is consistent with FTIR spectra (Fig. 3). Signatures of other types of carbonyl groups are also detected, e.g. the high-frequency resonance (16) assigned mainly to unconjugated aliphatic carboxyl groups. By applying a spectral fitting procedure (Larsson et al. 1999; Wickholm et al. 1998) shown in Fig. 4B, C and Fig. 2S, degradations of carbohydrates and lignin in archaeological wood were semi-quantitatively determined.

The integral area ratio of the resonance 14 and the resonance 13, $A_{154}/A_{148}$ could be used to recognize the wood as hardwood and softwood and to evaluate the depletion of the β-O-4 linkages (Proietti et al. 2011), see Table 2 and Table S3. In hardwood, $A_{154}/A_{148}$ is greater than 1, whereas in softwood this ratio is smaller than 1. This is confirmed by the values measured for the non-degraded recent wood *C9, C10* (hardwood) and *C12* (softwood). As listed in Table 2, the $A_{154}/A_{148}$ ratio values are similar for slightly deteriorated archaeological wood and non-degraded wood, demonstrating that β-O-4 linkages were not affected during a slight wood degradation, whereas the $A_{154}/A_{148}$ ratio is increased significantly for severely deteriorated archaeological wood (Fig. 4B, Fig. S2. The $A_{154}/A_{148}$ value of severely deteriorated archaeological softwood *C6* is e.g. 7.1, which would cause a false evaluation as hardwood. To use $A_{154}/A_{148}$ to distinguish archaeological hardwoods from softwoods without other information might not be applicable. In principle depletion of the β-O-4 linkages in archaeological wood, leads to decrease of the $A_{154}/A_{148}$ ratio (Proietti et al. 2011), but an increase of this ratio has been reported previously for archaeological wood (Łucejko et al. 2012; Zborowska et al. 2019). In accordance, the studied severely deteriorated archaeological wood *C1–C6* have increased $A_{154}/A_{148}$ ratio (Table 2), which would imply that the degradation of lignin is due to preferential loss of guaiacyl units, or the preferential demethoxylation of guaiacyl units (Łucejko et al. 2012; Zborowska et al. 2019; Lucejko et al. 2021).

This is consistent with the results of the FTIR measurements. Lignocellulosic degradation mechanisms are diverse and also depend on the various types of wood cell wall components (Cragg et al. 2015). For instance, it is reported that the guaiacyl units are more sensitive to artificial aging degradation processes than the syringyl units (Colom et al. 2003), whereas syringyl units have the higher biodegradability compared with the guaiacyl units (Proietti et al. 2011). This has to be taken into account in future studies.

Carbohydrates show significant differences in NMR spectra of archaeological wood with different preservation states. Carbon atoms of cellulose and hemicellulose have overlapped resonances in the range 105–65 ppm due to their chemical similarity. The ratio $A_{105}/A_{56}$ of resonance 9 at 105 ppm ($C_1$ of cellulose as reference) and resonance 2 at 56 ppm (methoxy group of lignin) (Alesiani et al. 2005; Wikberg and Maunu 2004), can be used to estimate the degradations of carbohydrates and lignin (Bardet et al. 2009). Non-degraded recent wood has $A_{105}/A_{56}$ ratios of about 1.0–1.5, while severely deteriorated

archaeological wood shows values < 0.4 (Table 2). This indicates that carbohydrates are degraded in considerably larger amounts than demethoxylation of lignin units in severely deteriorated archaeological wood. The $A_{105}/A_{56}$ ratio of slightly deteriorated archaeological wood *C8* with 4.7 is much higher than that of non-degraded wood of the same species *C12*. This is probably due to the demethoxylation of lignin units, as indicated by the weak intensity of resonance 5 and the good preservation of carbohydrates in slightly deteriorated archaeological wood (Fig. 4B, C8).

The NMR resonance at 89 ppm is assigned to $C_4$ in crystalline cellulose, whereas the signal at 84 ppm indicates amorphous cellulose or less ordered celluloses (Bardet et al 2009; Guo et al 2019; Larsson et al 1999; Spinella et al 2021; Wickholm et al. 1998; Wikberg and Maunu 2004). Both intensities decrease significantly in the spectra of severely deteriorated archaeological wood (Fig. 4C, Fig. S2). The crystalline/amorphous ratio of cellulose, $A_{89}/A_{84}$, which is often used to estimate the cellulose crystallinity, drops from 0.2 to 0.3 for non-degraded woods and slightly deteriorated archaeological woods to 0.02–0.11 for severely deteriorated archaeological woods, except for *C4* (Table 2). This could indicate degradation of not only surface chains but also inner chains in cellulose.

The intensity of resonance 8 at 89 ppm shows in the deconvoluted NMR spectra (Fig. 4C, Fig. S2) is weaker for samples *C1*, *C3* and *C6*, than that of *C2* and *C4*. Together with the information from sugar analysis, that the glucose content in *C1*, *C3,* and *C6* is less than that in *C2* and *C4* one can conclude, that among the degraded archaeological wood samples, cellulose in *C1*, *C3,* and *C6* were subject to more severe degradation. Sample *C8* does not show stronger resonance 8 and higher glucose content, indicating only slight degradation, which is in accordance with literature (Bardet et al. 2009). This implies that the crystal structure of cellulose is indeed different between severely deteriorated archaeological wood and slightly deteriorated archaeological wood.

These findings show that there was only a small amount of cellulose in severely deteriorated archaeological wood. Moreover, the lower carbohydrates to lignin ratio, significant loss of hemicellulose, partial decomposition of lignin, lower crystalline to amorphous cellulose ratio and a disordered molecular structure of cellulose were found.

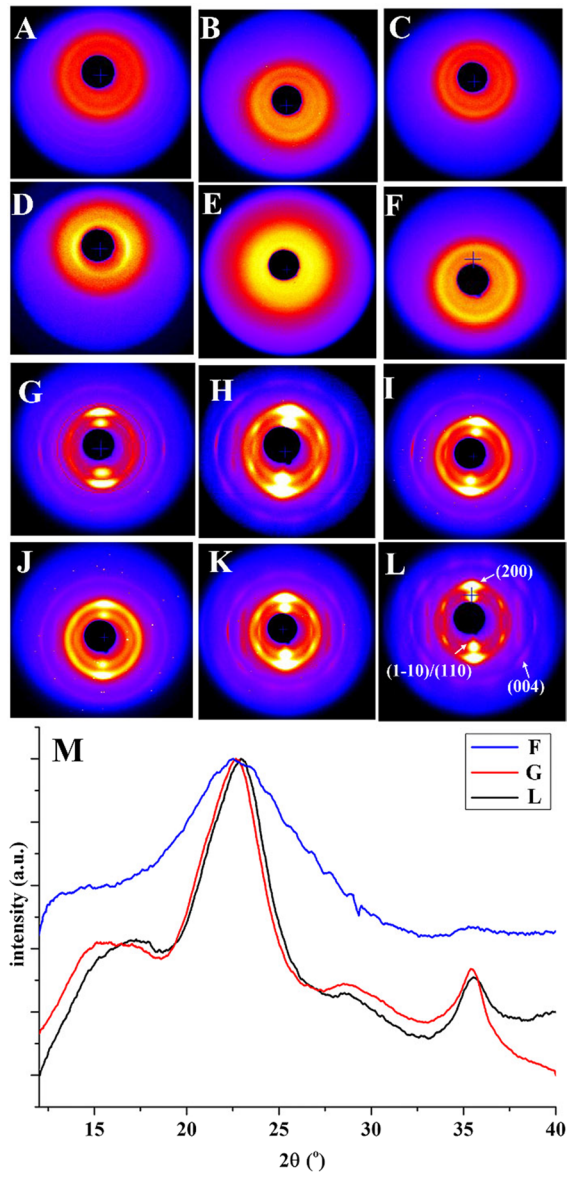


**Fig. 5** WAXD patterns of archaeological and recent wood, **A**: *C1*, **B**: *C2*, **C**: *C3*, **D**: *C4*, **E**: *C5*, **F**: *C6*, **G**: *C7*, **H**: *C8*, **I**: *C9*, **J**: *C10*, **K**: *C11*, **L**: *C12*. Multiple diffraction peaks from the cellulose nanofibrils (indexed as (1–10/110), (200), and (004)) are indicated. (M) WAXD curves of F, G, and L from the integration over the full azimuthal range

*Crystal structure of cellulose in archaeological wood from WAXD*

The crystal structure of cellulose in archaeological wood was analyzed by WAXD. Figure 5L depicts scattering of non-degraded wood (*C12*) with the crystalline peaks of cellulose I, (1–10)/(110) merged, (200), and (004), indicated. The respective scattering curve after full azimuthal integration is depicted in Fig. 5M, showing the peak positions clearly at about 17° 2θ, 22.9° 2θ and 35.7° 2θ, respectively. These typical cellulose peaks are present for slightly deteriorated (*C7*, *C8)* and recent wood *C9–C12,* see Fig. 5G–L. Severely deteriorated archaeological wood *C1–C6* does not show any orientation in the scattering signal (Fig. 5A–F), but faint rings, that might be identified with cellulose structure merged with the signal from amorphous contributions. The scattering curve features a very broad peak at around 22.5° 2θ, and a broad shoulder at around 35° 2θ, see Fig. 5M, blue curve indicated Fig. 5F. The main peak at 22.5° 2θ is not fully assigned to the amorphous cellulose since its peak position is generally found at angles of 18° 2θ (Segal 1959), smaller than 16° 2θ (Thygesen et al. 2005; Ju et al. 2015), 20°–21.5° 2θ (Agarwal et al. 2021; French 2020; Isogai & Atalla 1991), neither is it to the disordered carbonized cellulose at 17° 2θ nor to the disordered carbonized lignin at 21.2° 2θ (Meng et al. 2021). Sandak et. al. report on a higher amount of remaining crystal regions of cellulose with respect to amorphous regions, despite the fact of a low cellulose content (Sandak et al. 2010). Thus, considering the presence of crystalline cellulose at 89 ppm in solid state $^{13}C$ NMR spectra, although in small

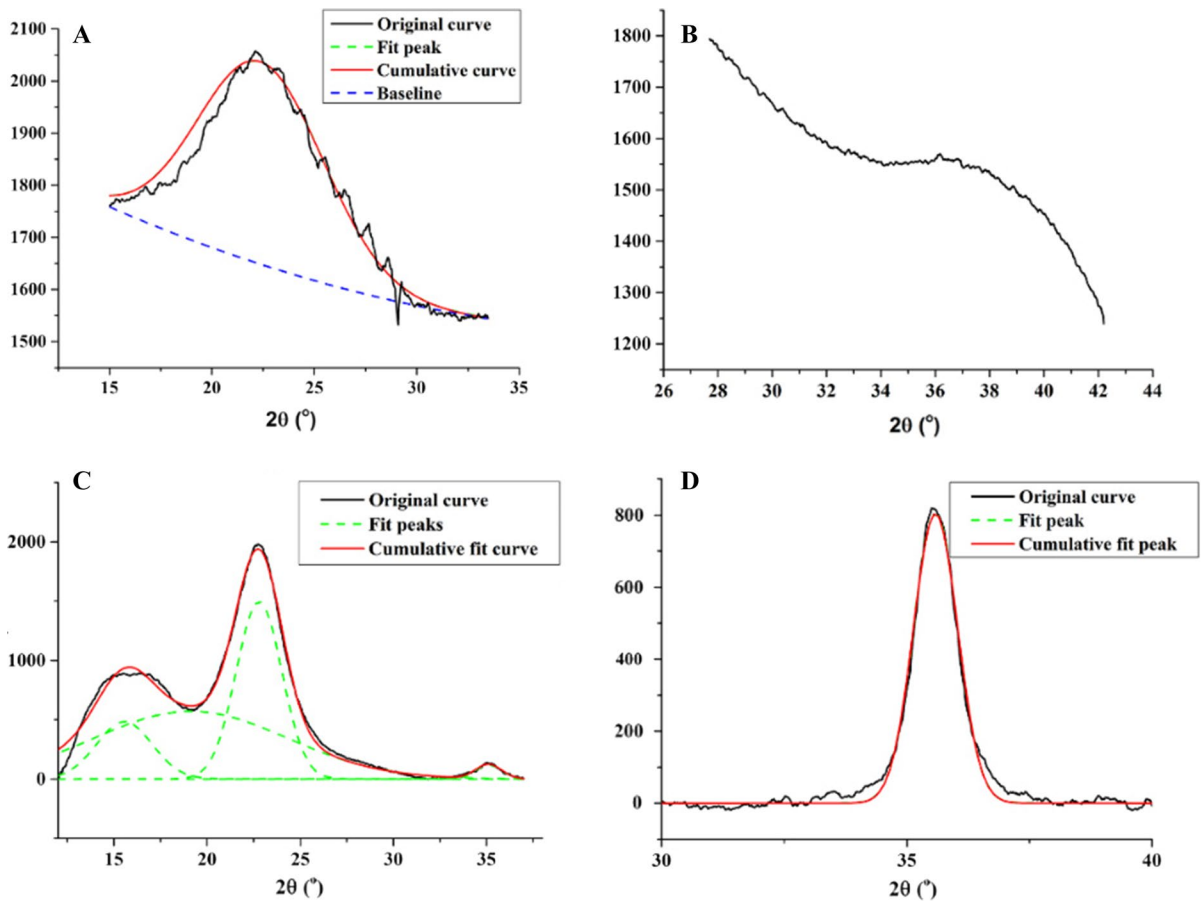


**Fig. 6** WAXD curves obtained via the selective integration of (200) of *C6* (**A**), (004) of *C6* (**B**), and (200) of *C7* (**C**), (004) of *C7* (**D**). Gaussian shaped curves were used for the peak fit. An exponential shaped curve was used for the baseline fit for severely deteriorated archaeological wood

**Table 4** Cellulosic crystal structure traits analyzed from the WAXD curves

| | WAXD | | | | | |
|---|---|---|---|---|---|---|
| | Peak position of (200) (°) | Interlattice spacing $d_{200}$ (nm) | Peak position of (004) (°) | Interlattice spacing $d_{004}$ (nm) | Crystallite size $L_{200}$ (nm) | Crystallite size $L_{004}$ (nm) |
| *C7* | 22.8 ± 0.1 | 0.390 ± 0.001 | 35.7 ± 0.3 | 0.252 ± 0.002 | 2.6 ± 0.08 | 7.7 ± 0.1 |
| *C8* | 22.9 ± 0.2 | 0.388 ± 0.004 | 35.7 ± 0.2 | 0.251 ± 0.002 | 2.4 ± 0.3 | 8.3 ± 0.3 |
| *C9* | 22.5 ± 0.1 | 0.395 ± 0.002 | 35.7 ± 0.5 | 0.251 ± 0.004 | 2.4 ± 0.04 | 7.0 ± 0.5 |
| *C10* | 22.6 ± 0.1 | 0.392 ± 0.002 | 35.6 ± 0.2 | 0.252 ± 0.001 | 2.4 ± 0.1 | 6.0 ± 0.1 |
| *C11* | 22.7 ± 0.1 | 0.391 ± 0.002 | 35.6 ± 0.2 | 0.252 ± 0.001 | 2.5 ± 0.05 | 6.9 ± 0.5 |
| *C12* | 22.9 ± 0.1 | 0.388 ± 0.002 | 35.7 ± 0.2 | 0.252 ± 0.001 | 2.6 ± 0.1 | 7.0 ± 0.4 |

quantity, and a certain amount of cellulose in severely deteriorated archaeological wood (Fig. 4C, Fig. S2, Table 2), the peak is assigned to the (200) reflection, allowing the assumption that a certain amount of the cellulose chains might be arranged into sheets. Nevertheless, it is evident that the crystal structure of cellulose was altered considerably in severely deteriorated archaeological wood.

The lack of the (110) and (1–10) reflection probably is due to several reasons, i.e. small crystallite size (Lin et al. 1985), very broad overlapping (200) peak and high amorphous contribution. Moreover, in contrast with slightly deteriorated archaeological wood, the (004) peak was not detected in severely deteriorated archaeological wood. The disappearance of the lattice planes (110), (1–10), and (004) were previously reported in the XRD patterns of cellulose nanocrystals from sugarcane peel (Abiaziem et al. 2020) and microcrystalline nitrocellulose from Alfa grass fibers (Trache et al. 2015). The vanishing of a clear (004) peak indicates disordered cellulose packing, because the (004) diffraction peak is sensitive to the alignment of the chains into fibrils, its loss has been also reported in defibrillated cellulose nanofibrils (Jiang et al. 2016).

To clearly resolve the (200) and (004) peaks, partial azimuthal integration was applied. Diffractograms together with peak analysis is depicted in Fig. 6. The peak position of the (200) and (004) reflections of all samples that could be evaluated are presented in Table 4. In general, the peaks are situated around 22.5–22.9° 2θ and are comparable for recent and slightly deteriorated wood, indicating maintained cellulose structure in this type of archaeological wood with lattice spacing of about 0.39 nm.

Although we suggest to assign the peak around 22.5° 2θ of severely deteriorated wood also to cellulose, peak evaluation is difficult, since amorphous

**Table 5** Cellulosic crystal structure traits analyzed from SAXS curves

| | | SAXS[a] | | | | | |
|---|---|---|---|---|---|---|---|
| | MFO (°) | $D_0$ (nm) | σ (nm) | $D_F$ (nm) | $l_{CH}^*$ (nm) | $R_g$ (nm) | n |
| *C1* | – | | | | 2.71 | 4.7 ± 0.1 | 3.1 ± 0.1 |
| *C2* | | | | | 2.65 | 4.5 ± 0.2 | 2.6 ± 0.2 |
| *C3* | | | | | 2.73 | 4.9 ± 0.1 | 3.1 ± 0.1 |
| *C4* | | | | | 2.63 | 5.2 ± 0.1 | 3.2 ± 0.1 |
| *C5* | | | | | 2.65 | 4.2 ± 0.1 | 2.5 ± 0.1 |
| *C6* | | | | | 2.64 | 4.3 ± 0.1 | 2.3 ± 0.1 |
| *C7* | 20 | 1.7 | 0.5 | 3.5 | 2.63 | 4.4 ± 0.1 | 2.7 ± 0.1 |
| *C8* | 19 | 1.6 | 0.8 | 3.4 | 2.63 | 4.3 ± 0.1 | 2.7 ± 0.1 |
| *C9* | 15 | 2.6 | 0.2 | 3.1 | 2.58 | 3.8 ± 0.1 | 1.9 ± 0.1 |
| *C10* | 17 | 2.7 | 0.1 | 3.4 | 2.59 | 4.4 ± 0.1 | 2.4 ± 0.1 |
| *C11* | 13 | 2.6 | 0.1 | 3.1 | 2.61 | 3.4 ± 0.1 | 2.0 ± 0.1 |
| *C12* | 11 | 2.5 | 0.2 | 2.8 | 2.66 | 3.6 ± 0.2 | 1.9 ± 0.1 |

[a]MFO: microfibril orientation distribution; $D_0$: the mean fibril diameter, which is in the direction perpendicular to the fibril axis. σ: the diameter distribution. $D_0$ and σ were calculated via the supplement material Fig. S2. $l_{CH}^*$: correlation length; $R_g$: radius of gyration; n: fractal dimension

contributions can not clearly be addressed by the fit (Fig. 6A) in the limited range of scattering angle, the peak was therefore not further considered for severely deteriorated wood (*C1–C6*). It shall nevertheless be stated, that the peak positions are also around 22.5° 2θ. The suggested existence of the (200) reflection also would mean that even towards severely deteriorated archaeological wood, the cellulose lattice perpendicular to the cellulose chain direction might still be maintained to a certain extent.

Slightly deteriorated archaeological wood and non-degraded recent wood show a small peak at 2θ of 35.5°, related to the (004) planes of the periodic structure of the crystallite along the axial direction with a lattice spacing of 0.25 nm.

The crystallite size of the cellulose crystals $L_{200}$ and $L_{004}$ were calculated by the Sherrer equation (Eq. 2) from the width of the corresponding diffraction peaks—the values are listed in Table 4. Recent wood and slightly decayed wood feature values of about $L_{200}=2.4$ nm and $L_{004}=7$ nm (*C9*). Also in this case, the detailed evaluation of severely deteriorated archaeological wood was omitted, but the broad peak (Fig. 5M, Fig. 6A) would indicate a drastically reduced crystallite size ($L_{200}$ of about 1 nm), with respect to slightly degraded archaeological or recent wood. The assumed reduced crystallite size for severely degraded archaeological wood also confirms a decrease in cellulose crystallinity (NMR) which is observed in advanced decay stages and is usually due to biodeterioration by e.g. bacteria and soft rot fungi.

Thus, in comparison with slightly deteriorated archaeological wood, severely deteriorated archaeological wood present similar but more striking changes. If any, there are much smaller non-arranged crystals and a much higher degree of amorphous cellulose. Cellulose crystallites would be fragmented along the cellulose chain direction, following a serious cellulose depolymerization.

*Microfibrils evaluation from SAXS*

The arrangement of cellulose fibrils can be quantified by measuring the angular distribution of microfibril orientations (MFO). The values of recent wood *C9–C12* were in the range of 11–17°, slightly deteriorated archaeological wood *C7* and *C8* showed values of 20° and 19°, respectively (Table 5). Severely deteriorated wood showed non-orientated scattering signal in the SAXS region (images not shown), similar to the isotropic orientation in WAXD (Fig. 5A–F), thus angle evaluation was not possible. These results might indicate that the arrangement of cellulose fibrils in archaeological wood became disordered, or vanished completely for severely deteriorated archaeological wood. Wide scatter of angular distributions in wood as a biological material has to be taken into account for interpretation. More samples for a statistical analysis would be advantageous.

The microfibril diameter was evaluated from the scattering curves, according to Jakob et al. (1994). Since the size of microfibrils is similar to the microfibril-to-microfibril distances, the form factor and the structure factor due to the arrangement of fibrils convolutes, which possibly influences fitting of actual values. To be comparable to literature, the evaluation is anyhow presented. The scattering curves I(q) for archaeological and recent wood are displayed in Fig. 7. The scattering curve is characteristic for the cellulose fibril structure and can be identified by the pronounced shoulder at about $q=1.4$ nm$^{-1}$ and a clear minimum at about $q=2.7$ nm$^{-1}$. The scattering

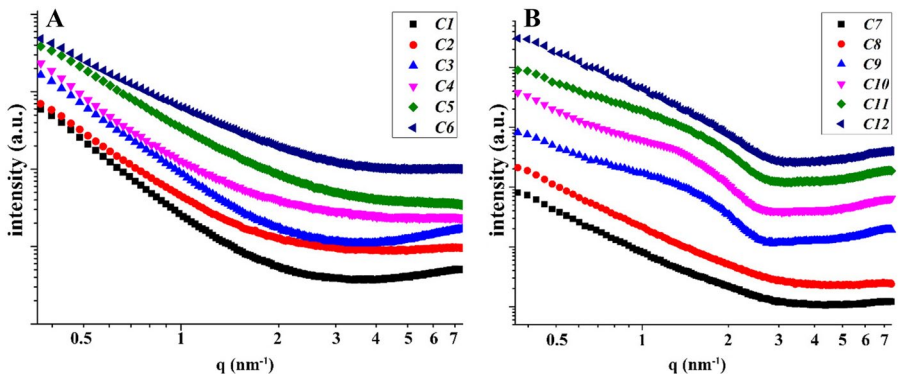


**Fig. 7** SAXS profiles of **A** severely deteriorated archaeological wood *C1 – C6*, **B** slightly deteriorated archaeological wood *C7*, *C8* and recent wood *C9 – C12*

curves of recent wood *C9–C12* indicate cellulose fibrillar structure, which is also visible in the scattering curves of *C7* and *C8* to a certain extent, while the features are not visible in the SAXS curves of *C1–C6*. From the position of the shoulder and the first minimum of the Bessel function (Fig. S3), the diameter of cellulose elementary fibrils $D_0$, the diameter distribution σ and the fibril distance $D_F$ could be obtained for samples *C7–C12*, which was not possible for the samples *C1–C6*. For recent wood, $D_F$, $D_0$ and σ values are about 2.8–3.4 nm, 2.6 nm, 0.2 nm, respectively, for slightly degraded wood, values are changed clearly, i.e. $D_F$, $D_0$ and σ values are about 1.7 nm, 3.4 nm and > 0.5 nm, respectively (Table 5). Even in slightly deteriorated archaeological wood, the SAXS curve is clearly smeared out (Fig. 7B), which was previously reported in archaeological wood samples from the Vasa (Svedström et al. 2012). This can also be ascribed to the wide diameter distribution of cellulose elementary fibrils, also visible in the fit results. Results show comparable $D_F$, smaller $D_0$ and a much larger σ than recent wood. The loss of clear scattering features reduced fibril diameter and increased diameter distribution are clear indications of cellulose fibril degradation resulting in disordered arrangement of cellulose at the fibrils surface. This could be expected from information about cellulose degradation from FTIR, NMR and sugar content analysis.

To address structure features also for severely deteriorated wood, the correlation length, $l_{CH}^*$ was used, which is closely connected with the shoulder features of the scattering intensities (Penttilä et al. 2013). The interfibrillar distance as an estimate of the intensity-averaged electron density fluctuations can thus be qualitatively described (Glatter and Kratky 1982; Ehmann et al. 2015). This is true for recent and slightly deteriorated wood, while for severely deteriorated wood, where no fibrillary structure is preserved this value rather refers to cellulose aggregates. As listed in Table 3, slightly deteriorated samples show a decrease in $l_{CH}^*$. In contrast, severely deteriorated samples show no clear trend. It is concluded that there are no typical cellulose aggregates in severely deteriorated archaeological wood.

Cracks and pores in the wood structure were studied at low scattering angles by a power law and the Guinier approximation. The power law exponent, n, is assigned to a mass fractal dimension when $\frac{5}{3} < n < 3$ and related to surface fractal dimension when $3 < n < 4$ (Teixeira 1988). While recent wood displays an average value of n = 2.0 and slightly deteriorated wood an average value of 2.7, severely deteriorated wood shows values up to 3.2 (Table 5). This indicates a considerable change in the fractal dimension of higher order cracks and pores. Degradation considerably affected the interface characteristics of archaeological wood on the nanoscale. The related pore size, $R_g$ was evaluated by the Guinier approximation. The $R_g$ ranges from 3.4 to 4.4 nm for recent wood of different species, 4.2 and 4.3 nm for slightly deteriorated archaeological wood, and 4.2–5.2 nm for severely deteriorated archaeological wood (Table 3). This means that the mean pore size among cellulose aggregates in severely deteriorated archaeological wood was larger compared to that of the respective recent wood of the same species, for all archaeological samples examined. It is in accordance with the increment of size and accumulated volume of mesopores in archaeological wood (Guo et al. 2019). The increased $R_g$, also proved a looser arrangement of cellulose aggregates in severely deteriorated archaeological wood, which could be caused by the

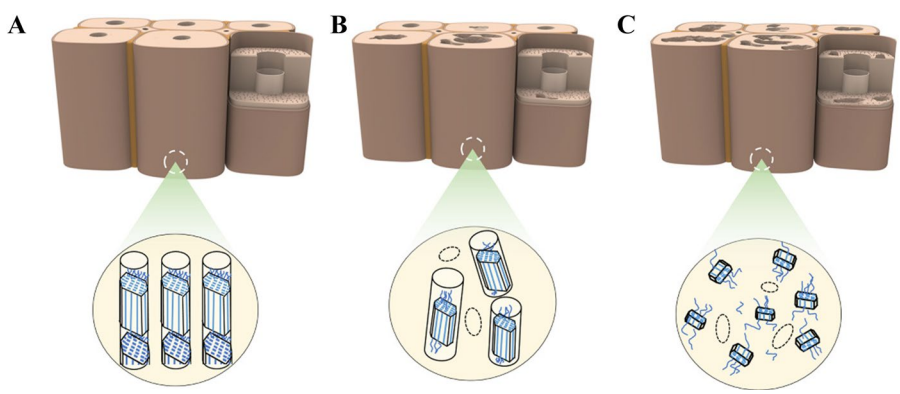


**Fig. 8** Proposed schemes for preserved cellulose in **A** non-degraded recent wood, **B** slightly deteriorated archaeological wood, **C** severely deteriorated archaeological wood

degradation of cell wall components (Jungnikl et al. 2008).

Overall it can be concluded, that a certain small amount of celluloses was likely preserved in severely deteriorated archaeological wood, featuring a lower carbohydrates and lignin ratio, a profound loss of hemicellulose, a serious degradation of cellulose in both amorphous and crystalline domains, a lower crystalline/amorphous ratio and more disordered cellulose molecular packing. Therefore, the well-known cellulose aggregates in recent wood being of crystalline nature and ordered in fibrillary arrangement, as shown in Fig. 8A, have been significantly changed after the severe degradation. Preserved cellulose of severely deteriorated archaeological wood is mainly amorphous but WAXD and NMR anyhow show indication of a certain amount of remaining crystallinity, featuring a small, but detectable NMR resonance at 89 ppm and an X-ray diffraction peak at (002) position. The (004) reflection vanished and WAXD and SAXS pattern show no orientation any more. It is speculated that cellulose crystallites were fragmented into cellulose crystalline lamellae after a serious cellulose degradation (Fig. 8C). Moreover, the smaller the crystal, the stronger is the influence of its more disordered surface (Müller et al. 2007). Cracks and pores are apparent in the severely deteriorated wood structure. Cellulose in slightly deteriorated archaeological wood was better preserved, having almost identical interlattice spacings, average fibril distance $D_F$ and the correlation length parameter with respect to non-degraded recent wood (Fig. 8B). Despite these structural features nearly intact, the decrease in the carbohydrates and lignin ratio, alterations in molecular structures of hemicellulose and lignin, still caused reduced fibril diameter $D_0$, increased pore size and altered interfaces, with respect to recent wood (Fig. 8).

## Conclusion

By application of several characterization methods the differences in cellulose hierarchical structure between slightly and severely deteriorated archaeological wood could be shown generally. The preservation state of wood can clearly be linked to the deterioration state of cellulosic structure from the crystalline level up to the microscopic level. Alterations in molecular structures of hemicellulose and lignin are the main cause of structural degradation, resulting in fragmentation of cellulose crystallites and cellulose microfibrils, opening of pores and loss of preferred orientations. Despite the advanced wood deterioration, in severely deteriorated wood samples, a certain amount of cellulose was preserved in severely deteriorated archaeological wood. For these samples a serious degradation of cellulose in both amorphous and crystalline domains, was found. Highly fragmented, mainly amorphous, but still in small fractions crystalline cellulose is assumed from the data. A broader study would be needed to fully clarify this point in the future. At last, it should be emphasized that waterlogged archaeological wood generally experienced a complicated degradation pathway due to many influencing factors during decay.

**Acknowledgments** Dr. Nannan Xiao from Institute of Biophysics, Department of Nanobiotechnology, University of Natural Resources and Life Sciences, Vienna is acknowledged for SEM samples preparation with the cryo-microtome. Mr Yonggang Zhang, Dr Mengyu Dong and Dr Ren Li from the Research Institute of Wood Industry, Chinese Academy of Forestry, China are acknowledged for the archaeological wood collection and the wood identification.

**Funding** This work is financially supported by "National Key R&D Program of China" (2020YFC1521800), the department of Science and Technology, National Forestry and Grassland Administration (2020132601) and the "Chinese National Natural Science" Foundation (31600450). Open access funding provided by University of Natural Resources and Life Sciences, Vienna (BOKU). The authors have not disclosed any funding.

**Declarations**

**Conflict of interest** The authors declare that we do not have any conflict of interest in submission of this manuscript.

## References


Abiaziem CV, Williams AB, Inegbenebor AI et al (2020) Isolation and characterisation of cellulose nanocrystal obtained from sugarcane peel. Rasayan J Chem 13(1):177–187. https://doi.org/10.31788/RJC.2020.1315328

Agarwal UP, Reiner RS, Ralph SA, Catchmark J, Chi K, Foster EJ, Hunt CG, Baez C, Ibach RE, Hirth KC (2021) Characterization of the supramolecular structures of cellulose nanocrystals of different origins. Cellulose 28(3):1369–1385. https://doi.org/10.1007/s10570-020-03590-z

Alesiani M, Proietti F, Capuani S et al (2005) $^{13}$C CPMAS NMR spectroscopic analysis applied to wood characterization. App Magn Reson 29:177–184. https://doi.org/10.1007/BF03167005

Almkvist G, Norbakhsh S, Bjurhager I et al (2016) Prediction of tensile strength in iron-contaminated archaeological wood by FT-IR spectroscopy–a study of degradation in recent oak and *Vasa* oak. Holzforschung 70:855–865. https://doi.org/10.1515/hf-2015-0223

Anagost SE, Worrall JJ, Wang CJK (1994) Diffuse cavity formation in soft rot of pine. Wood Sci Technol 28:199–208. https://doi.org/10.1007/BF00193328

Bardet M, Gerbaud G, Giffard M et al (2009) $^{13}$C high-resolution solid-state NMR for structural elucidation of archaeological woods. Prog Nucl Mag Res Sp 55(3):199–214. https://doi.org/10.1016/j.pnmrs.2009.02.001

Bjurhager I, Halonen H, Lindfors E et al (2012) State of degradation in archeological oak from the 17th century Vasa ship: substantial strength loss correlates with reduction in (holo)cellulose molecular weight. Biomacromol 13:2521–2527. https://doi.org/10.1021/bm3007456

Blanchette RA (2000) A review of microbial deterioration found in archaeological wood from different environments. Int Biodeter Biodegr 46(3):189–204. https://doi.org/10.1016/S0964-8305(00)00077-9

Breßler I, Kohlbrecher J, Thünemann AF (2015) SASfit: a tool for small-angle scattering data analysis using a library of analytical expressions. J Appl Cryst 48:1587–1598. https://doi.org/10.1107/S1600576715016544

Broda M, Popescu C (2019) Natural decay of archaeological oak wood versus artifice-al degradation processes–an FT-IR spectroscopy and X-ray diffraction study. Spectrochim Acta A 209:280–287. https://doi.org/10.1016/j.saa.2018.10.057

Cavallaro G, Gallitto AA, Lisuzzo L et al (2019) Comparative study of historical woods from XIX century by thermogravimetry coupled with FTIR spectroscopy. Cellulose 26:8853–8865. https://doi.org/10.1007/s10570-019-02688-3

Colom X, Carrillo F, Nogués F et al (2003) Structural analysis of photodegraded wood by means of FTIR spectroscopy. Polym Degrad Stabil 80:543–549. https://doi.org/10.1016/S0141-3910(03)00051-X

Colombini MP, Lucejko JJ, Modugno F et al (2009) A multianalytical study of degradation of lignin in archaeological waterlogged wood. Talanta 80:61–70. https://doi.org/10.1016/j.talanta.2009.06.024

Committee IAWA (2004) IAWA list of microscopic features for softwood identification. IAWA J 25(1):1–70

IAWA Committee (1989) IAWA list of microscopic features for hardwood identification. IAWA Bulletin n.s.: Leiden.

Conard NJ, Serangeli J, Bigga G et al (2020) A 300,000-year-old throwing stick from Schöningen, northern Germany, documents the evolution of human hunting. Nat Ecol Evol 4:690–693. https://doi.org/10.1038/s41559-020-1139-0

Cragg SM, Beckham GT, Bruce NC et al (2015) Lignocellulose degradation mechanisms across the tree of life. Curr Opin Chem Biol 29:108–119. https://doi.org/10.1016/j.cbpa.2015.10.018

Darwish SS, El Hadidi NMN, Mansour M (2013) The effect of fungal decay on *Ficus Sycomorus* wood. Int J Conser Sci 4(3):271–282

Ehmann HMA, Werzer O, Pachmajer S et al (2015) Surface-sensitive approach to interpreting supramolecular rearrangements in cellulose by synchrotron grazing Incidence Small-Angle X-ray Scattering. ACS Macro Lett 4:713–716. https://doi.org/10.1021/acsmacrolett.5b00306

Evershed RP, Jerman K, Eglinton G (1985) Pine wood origin for pitch from t-he *Mary Rose*. Nature 314:528–530. https://doi.org/10.1038/314528a0

Faix O (1991) Classification of lignins from different botanical origins by FT-IR spectroscopy. Holzforschung 42:21–27. https://doi.org/10.1515/hfsg.1991.45.s1.21

French AD (2020) Increment in evolution of cellulose crystallinity analysis. Cellulose 27:5445–5448. https://doi.org/10.1007/s10570-020-03172-z

Garusinghe UM, Raghuwanshi VS, Garvey CJ et al (2017) Assembly of nanoparticles-polyelectrolyte complexes in nanofiber cellulose structures. Colloid Surface A 513:373–379. https://doi.org/10.1016/j.colsurfa.2016.10.068

Geng W, Narron R, Jiang X et al (2019) The influence of lignin content and structure on hemicellulose alkaline extraction for non-wood and hardwood lignocellulosic biomass. Cellulose 26:3219–3230. https://doi.org/10.1007/s10570-019-02261-y

Ghavidel A, Hosseinpourpia R, Militz H et al (2020) Characterization of archaeological european white elm (*Ulmus laevis* .P) and black poplar (*Populus nigra* L.). Forests 11:1329. https://doi.org/10.3390/f11121329

Giachi G, Bettazzi F, Chimichi S et al (2003) Chemical characterization of degraded wood in ships discovered in a recent excavation of the Etruscan and Roman harbor of Pisa. J Cult Herit 4(2):75–83. https://doi.org/10.1016/S1296-2074(03)00018-9

Glatter O, Kratky O (1982) Small angle X-ray scattering. Academin Press, London

Glausiusz J (2020) Wood–the vein that runs through human history. Nature 588:26–27. https://doi.org/10.1073/pnas.1108942108

Guinier A, Fournet G (1955) Small-angle scattering of X-rays. Wiley, New York

Guo J, Rennhofer H, Yin Y (2016) The influence of thermo-hygro-mechanical treatment on the micro- and nanoscale architecture of wood cell walls using small- and wide-angle X-ray scattering. Cellulose 23:2325–2340. https://doi.org/10.1007/s10570-016-0982-2

Guo J, Xiao L, Han L et al (2019) Deterioration of the cell wall in waterlogged wooden archeological artifacts, 2400 years

old. IAWA J 40:820–844. https://doi.org/10.1163/22941932-40190241

Guo J, Zhang M, Liu J et al (2020) Evaluation of the deterioration state of archaeological wooden artifacts: a nondestructive protocol based on direct analysis in real time–mass spectrometry (DART-MS) coupled to chemometrics. Anal Chem 92:9908–9915. https://doi.org/10.1021/acs.analchem.0c01429

Han L, Tian X, Keplinger T et al (2020a) Even visually intact cell walls in waterlogged archaeological wood are chemically deteriorated and mechanically fragile: a case of a 170-year-old shipwreck. Molecules 25(5):1113. https://doi.org/10.3390/molecules25051113

Han L, Guo X, Wang K et al (2020b) Hygroscopicity of waterlogged archaeological wood from Xiaobaijiao No.1 Shipwreck related to its deterioration state. Polymers 12(4):834. https://doi.org/10.3390/polym12040834

High KE, Penkman KEH (2020) A review of analytical methods for assessing preservation in waterlogged archaeological wood and their application in practice. Herit Sci 8(1):83. https://doi.org/10.1186/s40494-020-00422-y

Howell C, Hastrup ACS, Jellison J (2007) The use of X-ray diffraction for analyzing biomodification of crystalline cellulose by wood decay fungi. International Research Group on Wood Protection. IRG/WP, 07-10622, Conference Proceeding, Jackson, USA

Isogai A, Atalla RH (1991) Amorphous celluloses stable in aqueous media: regeneration from $SO_2$–amine solvent systems. J Polym Sci Part A: Polym Chem 29(1):113–119. https://doi.org/10.1002/pola.1991.080290113

Jakob HF, Fratzl P, Tschegg SE (1994) Size and arrangement of elementary cellulose fibrils in wood cells: a small-angle X-ray scattering study of *Picea abies*. J Struct Biol 113:13–22. https://doi.org/10.1006/jsbi.1994.1028

Jakob HF, Fengel D, Tchegg SE et al (1995) The elementary cellulose fibril in *Picea abies*: Comparison of transmission electron microscopy, small-angle X-ray scattering, and wide-angle X-ray scattering results. Macromolecules 28:8782–8787. https://doi.org/10.1021/ma00130a010

Jiang F, Kondo T, Hsieh Y (2016) Rice straw cellulose nanofibrils via aqueous counter collision and differential centrifugation and their self-assembled structures. ACS Sustain Chem Eng 4(3):1697–1706. https://doi.org/10.1021/acssuschemeng.5b01653

Ju X, Bowden M, Brown EE, Zhang X (2015) An improved X-ray diffraction method for cellulose crystallinity measurement. Carbohydr Polym 123:476–481. https://doi.org/10.1016/j.carbpol.2014.12.071

Jungnikl K, Paris O, Fratzl P et al (2008) The implication of chemical extraction treatments on the cell wall nanostructure of softwood. Cellulose 15:407–418. https://doi.org/10.1007/s10570-007-9181-5

Kennedy CJ, Cameron GJ, Šturcová A et al (2007) Microfibril diameter in celery collenchyma cellulose: X-ray scattering and NMR evidence. Cellulose 14:235–246. https://doi.org/10.1007/s10570-007-9116-1

Larsson PT, Hult E, Wickholm K et al (1999) CP/MAS $^{13}$C-NMR spectroscopy applied to structure and interaction studies on cellulose I. Solid State Nucl Mag 15:31–40. https://doi.org/10.1016/S0926-2040(99)00044-2

Larsson PT, Stevanic-Srndovic J, Roth SV et al (2022) Interpreting SAXS data recorded on cellulose rich pulps. Cellulose 29:117–131. https://doi.org/10.1007/s10570-021-04291-x

Li M, Fang B, Zhao Y et al (2014) Investigation into the deterioration process of archaeological bamboo strips of China from four different periods by chemical and anatomical analysis. Polym Degrad Stabil 109:71–78. https://doi.org/10.1016/j.polymdegradstab.2014.06.022

Lichtenegger H, Reiterer A, Stanzl-Tschegg SE et al (1999) Variation of cellulose microfibril angles in softwoods and hardwoods–a possible strategy of mechanical optimization. J Struct Biol 128:257–269. https://doi.org/10.1006/jsbi.1999.4194

Lin FC, Brown RM, Cooper JB et al (1985) Synthesis of fibrils in vitro by a solubilized cellulose synthase from *Acetobacter xylinum*. Science 230(4727):822–825. https://doi.org/10.1126/science.230.4727.822

Liu B, Wang N, Chen M et al (2017) Earliest hydraulic enterprise in China, 5,100 years ago. PNAS 114:13637–13642. https://doi.org/10.1073/pnas.1710516114

Łucejko JJ, Zborowska M, Modugno F et al (2012) Analytical pyrolysis vs. classical wet chemical analysis to assess the decay of archaeological waterlogged wood. Anal Chim Acta 745:70–77. https://doi.org/10.1016/j.aca.2012.07.046

Lucejko JJ, Tamburini D, Zborowska M et al (2020) Oak wood degradation processes induced by the burial environment in the archaeological site of Biskupin (Poland). Herit Sci 8:44. https://doi.org/10.1186/s40494-020-00390-3

Lucejko JJ, Tamburini D, Modugno F et al (2021) Analytical pyrolysis and mass spectrometry to characterise lignin in archaeological wood. Appl Sci 11:240. https://doi.org/10.3390/app11010240

Macchioni N, Pizzo B, Capretti C et al (2012) How an integrated diagnostic approach can help in a correct evaluation of the state of preservation of waterlogged archaeological artefacts. J Archaeol Sci 39:3255–3263. https://doi.org/10.1016/j.jas.2012.05.008

Meng Y, Contescu CI, Liu P et al (2021) Understanding the local structure of disordered carbons from cellulose and lignin. Wood Sci Technol 55(3):587–606. https://doi.org/10.1007/s00226-021-01286-6

Müller M, Murphy B, Burghammer B et al (2007) Aging of native cellulose fibres under archaeological conditions: textiles from the dead sea region studied using synchrotron X-ray microdiffraction. Appl Phys A 89:877–881. https://doi.org/10.1007/s00339-007-4219-y

Nevin A, Sawicki M (2019) Heritage wood. Investigation and conservation of art on wood, Springer, Switzerland

Nishiyama Y, Langan P, Chanzy H (2002) Crystal structure and hydrogen-bonding system in cellulose I$\beta$ from synchrotron X-ray and neutron fiber diffraction. J Am Chem Soc 124:9074–9082. https://doi.org/10.1021/ja0257319

Pandey KK, Pitman AJ (2003) FTIR studies of the changes in wood chemistry following decay by brown-rot and white-rot fungi. Int Biodeter Biodegr 52:151–160. https://doi.org/10.1016/S0964-8305(03)00052-0

Pedersen NB, Łucejko JJ, Modugno F et al (2021) Correlation between bacterial decay and chemical changes in waterlogged archaeological wood analysed by light microscopy

and Py-GC/MS. Holzforschung 75(7):635–645. https://doi.org/10.1515/hf-2020-0153

Penttilä PA, Várnai A, Fernández M et al (2013) Small-angle scattering study of structural changes in the microfibril network of nanocelulose during enzymatic hydrolysis. Cellulose 20:1031–1040. https://doi.org/10.1007/s10570-013-9899-1

Pizzo B, Pecoraro E, Alves A (2015) Quantitative evaluation by attenuated total reflectance infrared (ATR-FTIR) spectroscopy of the chemical composition of decayed wood preserved in waterlogged conditions. Talanta 31:14–20. https://doi.org/10.1016/j.talanta.2014.07.062

Pournou A (2020) Biodeterioration of wooden cultural heritage. Organisms and decay mechanisms in aquatic and terrestrial ecosystems. Springer, Switzerland.

Pozhidaev VM, Retivov VM, Panarina EI et al (2019) Development of a method for identifying wood species in archaeological materials by IR spectroscopy. J Anal Chem 74(12):1192–1201. https://doi.org/10.1134/S1061934819120104

Proietti N, Presciutti F, Tullio VD et al (2011) Unilateral NMR, 13C CPMAS NMR spectroscopy and micro-analytical techniques for studying the materials and state of conservation of an ancient Egyptian wooden sarcophagus. Anal Bioanal Chem 399:3117–3131

Romagnoli M, Galotta G, Antonelli F et al (2018) Micromorphological, physical and thermogravimetric analyses of waterlogged archaeological wood from the prehistoric village of Gran Carro (Lake Bolsena-Italy). J Cult Herit 33:30–38. https://doi.org/10.1016/j.culher.2018.03.012

Sandak A, Sandak J, Zborowska M et al (2010) Near infrared spectroscopy as a tool for archaeological wood characterization. J Archaeol Sci 37(9):2093–2101. https://doi.org/10.1016/j.jas.2010.02.005

Sarkanen KV, Chang H, Ericsson B (1967) Species variation in lignins I. Infrared spectra of guaiacyl and syringyl models. TAPPA J 50(11):572–575

Segal L, Creely JJ, Martin AE, Conrad CM (1959) An empirical method for estimating the degree of crystallinity of native cellulose using the X-ray diffractometer. Text Res J 29(10):786–794. https://doi.org/10.1177/004051755902901003

Sluiter A, Hames B, Ruiz R et al (2012) Determination of structural carbohydrates and lignin in biomass. Laboratory Analytical Procedure, version 08-03-2012

Spinella A, Martino DFC, Saladino ML et al (2021) Solid state NMR investigation of the roman Acqualadroni rostrum: tenth year assessment of the consolidation treatment of the wooden part. Cellulose 28:1025–1038. https://doi.org/10.1007/s10570-020-03563-2

Svedström K, Bjurhager I, Kallonen A et al (2012) Structure of oak wood from the Swedish warship Vasa revealed by X-ray scattering and microtomography. Holzforschung 66:355–363. https://doi.org/10.1515/hf.2011.157

Teixeira JJ (1988) Small-angle scattering by fractal systems. J Appl Crystallogr 21:781–785. https://doi.org/10.1107/S0021889888000263

Terrett OM, Lyczakowski JJ, Yu L et al (2019) Molecular architecture of softwood revealed by solid-state NMR. Nat Commun 10:4978. https://doi.org/10.1038/s41467-019-12979-9

Thygesen A, Oddershede J, Lilholt H et al (2005) On the determination of crystallinity and cellulose content in plant fibres. Cellulose 12:563–576. https://doi.org/10.1007/s10570-005-9001-8

Trache D, Khimeche K, Mezroua A et al (2015) Physicochemical properties of microcrystalline nitrocellulose from Alfa grass fibres and its thermal stability. J Therm Anal Calorim 124:1485–1496. https://doi.org/10.1007/s10973-016-5293-1

Traoré M, Kaal J, Cortizas AM (2016) Application of FTIR spectroscopy to the characterization of archaeological wood. Spectrochim Acta A 153:63–70. https://doi.org/10.1016/j.saa.2015.07.108

Wickholm K, Larsson PT, Iversen T (1998) Assignment of non-crystalline forms in celluloseI by CP/MAS $^{13}$C NMR spectroscopy. Carbohyd Res 312(3):123–129. https://doi.org/10.1016/S0008-6215(98)00236-5

Wikberg H, Maunu SL (2004) Characterisation of thermally modified hard- and softwoods by 13C CPMAS NMR. Carbohydr Polym 58(4):461–466. https://doi.org/10.1016/j.carbpol.2004.08.008

Zborowska M, Babiński L, Czaczyk K et al (2019) Evaluation of the rate of wood degradation at the iron age archaeological site of Biskupin. Poland Archaeom 62(1):141–156. https://doi.org/10.1111/arcm.12504

Zhou Y, Wang K, Hu D et al (2018) Degradation features of archaeological wood surface to deep inside a case study on wooden boards of Marquis of Haihun's outer coffin. Wood Res 63(3):419–430

Zoia L, Tamburini D, Orlandi M et al (2017) Chemical characterization of the whole plant cell wall of archaeological wood: an integrated approach. Anal Bioanal Chem 409:4233–4245. https://doi.org/10.1007/s00216-017-0378-7